



A02-13547

AIAA 2002-0151  
Receptivity of Görtler Vortices  
In Hypersonic Boundary Layers

Chong W. Whang and Xiaolin Zhong  
University of California, Los Angeles  
Los Angeles, CA

**40th Aerospace Sciences  
Meeting & Exhibit**  
January 14–17, 2002 / Reno, NV

# Receptivity of Görtler Vortices in Hypersonic Boundary Layers

Chong W. Whang \*and Xiaolin Zhong †

University of California, Los Angeles, California 90095

## Abstract

Görtler vortices appear in boundary layer flow along the concave surfaces due to the imbalance between pressure and centrifugal force. Many practical engineering designs involve concave surfaces such as engine inlet. In hypersonic boundary layers, there exist higher harmonic boundary layer modes (second, third mode etc.) as well as the first mode. If the flow is associated with the concave surfaces, Görtler mode also exists. Finding the most dominant instability mode in boundary layer flows is one of the fundamental problems in fluid mechanics. Forcing disturbances initially enter the boundary layers and generate instability waves which is called receptivity. Receptivity to free stream disturbances introduces random disturbances into the boundary layers, and the most dominant instability mode develops. It helps to find the most dangerous instability wave in boundary layers. In this paper, receptivity of Görtler and other instability waves in hypersonic boundary layers are investigated using Direct Numerical Simulation(DNS). Forcing disturbances are introduced into the hypersonic boundary layers by receptivity to free stream disturbances and blowing and suction. Random disturbances introduced by freestream acoustic and vorticity waves and blowing and suction develops Görtler kinds instability waves inside hypersonic boundary layers in concave region.

## 1 Introduction

Longitudinal counter rotating vortices appear in boundary layer flow along the concave surface. These vortices are called Görtler vortices and affect the flow instability in boundary layers along the concave surface. Görtler vortices have been studied experimentally and numerically since Görtler found them in 1940 [1-17]. Görtler vortices were observed experimentally by Tani [2] in 1962. In his low speed wind tunnel experiment, he observed spanwise variations of stream-

wise velocity along the concave wall. He found that the induced vortex wavelength is independent of the streamwise location and nearly independent of the free stream speed. Aihara [3] showed that the nonlinear development of Görtler vortices mainly affects the transition of the boundary layers. He imposed artificial impulsive disturbances on the existence of Görtler vortices. He found that the imposed disturbances amplify or decay in the linear region of Görtler vortices depending on the initial value of the excitation, but the disturbances rapidly grow in the nonlinear region. Peerhossaini and Wesfreid [4] observed that unsteady oscillations appear in steady Görtler vortices.

Recent experiments have shown that the breakdown of Görtler vortices is mainly due to the secondary instabilities. Aihara and Kohama [5] and Aihara et al [6] showed that the breakdown of the Görtler vortex structure into a horseshoe-vortex structure because of the secondary instability. Swearingen and Blackwelder [7] identified the two kinds of secondary instabilities to be the sinuous and varicose (horseshoe) types. They showed that the sinuous mode is produced by spanwise velocity gradient, and the varicose is due to normal velocity gradient. In their experiments, the unsteady secondary instability fluctuations were mainly the sinuous mode. They concluded that the sinuous mode plays a more important role in transition to turbulence of Görtler vortices.

Recently many researchers have investigated nonlinear Görtler problems numerically. Hall [8] numerically integrated the nonlinear partial differential equations for finite wave number of the vortices and demonstrated that nonlinear evolution of streamwise Görtler vortices produces inflectional profiles which may presumably break down. Lee and Liu [9] simulated spatially growing longitudinal vortices by a finite difference algorithm in solving the three-dimensional parabolized Navier-Stokes equations. Their results compared well with those from Swearingen and Blackwelder [7].

Liu and Domaradzki [10], Yu and Liu [11], and Li and Malik [12] studied secondary instability effects on Görtler vortices. Liu and Domaradzki [10] solved the full three-dimensional Navier-Stokes equations to investigate transition to turbulence of Görtler vortices.

\*Graduate Student, chong@seas.ucla.edu

†Associate Professor, Mechanical and Aerospace Engineering Department, Associate Fellow AIAA

Their flow conditions were the same as those by Swearingen and Blackwelder [7]. Initial disturbances were obtained from LST. They showed that Görtler vortices become turbulent due to the spanwise velocity gradient as well as the normal velocity gradient. These velocity profiles contain inflection points which affect the flow instabilities in boundary layers. They showed that the varicose mode is related to the normal velocity gradient, and the sinuous mode is to the spanwise gradient and concluded that the sinuous mode dominates the varicose. Li and Malik [12] used two-dimensional LST and three-dimensional PSE (parabolic stability equation) methods and studied nonlinear secondary instability effects on Görtler vortices. In their approaches, they showed there are two kinds of the secondary instability modes; even and odd. The even mode is related to the varicose mode, and the odd mode is to the sinuous mode. Their linear stability analysis showed that for the large wave length of Görtler vortices, the even modes are dominant, and for the short wave length, the odd modes have main roles for transition. They explained that it is the reason why some experiments [5][6] showed a varicose mode dominant break-down, but other experiment [7] showed a sinuous mode.

Nayfeh [13], in his multiple-scale analysis for two dimensional boundary layers, showed that Görtler vortices can interact with the oblique Tollmien-Schlichting (TS) waves whose spanwise wavelength is the twice of the vortices. He found that Görtler vortices strongly destabilize the TS waves. Malik [14] obtained the results which are not agreed with Nayfeh. He found the inconsistent length scale in Nayfeh's formula and showed in his temporal and parallel analysis that the oblique TS waves whose wavelength is the half of the vortices are destabilized by the nonlinear interaction. Nayfeh and Al-Maaitah [15] corrected the formula and presented the new results which are the same to Malik [14]. They used both Floquet theory and the method of multiple-scale and showed both methods give a good agreement. Malik and Hussaini [16] considered nonlinear interaction between two dimensional TS waves and Görtler vortices. In the analysis, incompressible Navier-Stokes equations are solved using a Fourier-Chebyshev spectral method. It is shown that the TS waves can be excited by Görtler vortices, and due to the nonlinear effects, Görtler vortices induces the oblique wave whose wavelength is the equal to the vortices.

There are many difficulties in the experimental studies of high speed receptivity phenomena. For example, it is difficult to generate controllable disturbances with a well defined and independently variable frequency. Therefore, Direct Numerical Simulation becomes an

useful tool in order to investigate supersonic and hypersonic receptivity process. Lin et al [18] solved compressible linearized Navier-Stokes equations and studied the receptivity of hypersonic boundary layer to different external disturbances. Zhong [19] studied the acoustic receptivity of hypersonic flow over blunt wedge by solving the full Navier-Stokes equations. It was shown that the interaction of free stream acoustic wave with bow shock generate instability waves behind the shock. Recently receptivity becomes a critical issue for the Görtler problem. Denier et al [17] addressed receptivity issue by considering the vortex motion induced by wall roughness.

## 2 FORMULATION

Governing equations and numerical methods for linear stability theory and direct numerical simulation are discussed in this chapter. For LST analysis, the full linearized compressible Navier-Stokes equations in cartesian coordinate system are derived. Wall curvature effects are included in LST analysis using a coordinate transformation. In the numerical simulation, the full Navier-Stokes equations are solved using a fifth order explicit upwind shock fitting scheme. Governing equations and numerical methods for the linear stability analysis and the numerical simulation are explained as follow.

### 2.1 Linear Stability Analysis

The compressible linear stability equations originate from the compressible Navier-Stokes equations. The gas is assumed to be perfect Newtonian gas. The three-dimensional Navier-Stokes equations in cartesian coordinates  $(x^*, y^*, z^*)$  are

$$\rho^* \left[ \frac{\partial \mathbf{u}^*}{\partial t^*} + \mathbf{u}^* \cdot \nabla \mathbf{u}^* \right] = -\nabla p^* + \nabla \cdot [\lambda^* (\nabla \cdot \mathbf{u}^*) \mathbf{I} + \mu^* (\nabla \mathbf{u}^* + \nabla \mathbf{u}^{*tr})], \quad (1)$$

$$\frac{\partial \rho^*}{\partial t^*} + \nabla \cdot (\rho^* \mathbf{u}^*) = 0, \quad (2)$$

$$\rho^* c_p^* \left[ \frac{\partial T^*}{\partial t^*} + \mathbf{u}^* \cdot \nabla T^* \right] = \nabla \cdot (k^* \nabla T^*) + \frac{\partial p^*}{\partial t^*} + \mathbf{u}^* \cdot \nabla p^* + \Phi^*, \quad (3)$$

$$p^* = \rho^* R^* T^*, \quad (4)$$

where '\*' denotes dimensional quantities.  $\mathbf{u}^*$  is the velocity vector,  $\rho^*$  is the density,  $p^*$  is the pressure,  $T^*$

is the temperature,  $R^*$  is the gas constant,  $c_p^*$  is the specific heat at constant pressure,  $k^*$  is the thermal conductivity,  $\mu^*$  is the first coefficient of viscosity, and  $\lambda^*$  is the second coefficient of viscosity. The viscosity coefficient is determined by Sutherland's law. The viscous dissipation function,  $\Phi^*$ , is given as

$$\Phi^* = \lambda^*(\nabla \cdot \mathbf{u}^*)^2 + \frac{\mu^*}{2}[\nabla \mathbf{u}^* + \nabla \mathbf{u}^{*tr}]^2. \quad (5)$$

The flow variables and equations are nondimensionalized as follows: velocity by  $U_\infty^*$ , density by  $\rho_\infty^*$ , pressure by  $\rho_\infty^* U_\infty^{*2}$ , length scales by  $x^*$ , and time scale by  $x^*/U_\infty^*$  where  $x^*$  denotes a distance from the leading edge. Instantaneous flow variables are represented as the sum of mean value and fluctuation, i.e.

$$q = \bar{q} + \tilde{q} \quad (6)$$

where  $\tilde{\mathbf{q}} = \{\tilde{u}, \tilde{v}, \tilde{p}, \tilde{T}, \tilde{w}\}^{tr}$ . All matrix coefficients are function of mean values.

A coordinate transformations is applied to transform cartesian coordinate (x,y,z) into curve linear system ( $\xi, \eta, \zeta$ ). Resulting linear disturbance equations can be expressed in matrix form as

$$\begin{aligned} & [A']\tilde{\mathbf{q}}_1 + [B']\frac{\partial \tilde{\mathbf{q}}_1}{\partial \tau} + [C']\frac{\partial \tilde{\mathbf{q}}_1}{\partial \xi'} + [D']\frac{\partial \tilde{\mathbf{q}}_1}{\partial \eta'} \\ & + [E']\frac{\partial \tilde{\mathbf{q}}_1}{\partial \zeta'} + [F']\frac{\partial^2 \tilde{\mathbf{q}}_1}{\partial \xi'^2} + [G']\frac{\partial^2 \tilde{\mathbf{q}}_1}{\partial \eta'^2} + [H']\frac{\partial^2 \tilde{\mathbf{q}}_1}{\partial \zeta'^2} \\ & + [I']\frac{\partial^2 \tilde{\mathbf{q}}_1}{\partial \xi' \partial \eta'} + [J']\frac{\partial^2 \tilde{\mathbf{q}}_1}{\partial \eta' \partial \zeta'} + [L']\frac{\partial^2 \tilde{\mathbf{q}}_1}{\partial \xi' \partial \zeta'} = 0, \quad (7) \end{aligned}$$

where  $\tilde{\mathbf{q}}_1 = \{\tilde{u}', \tilde{v}', \tilde{p}', \tilde{T}', \tilde{w}'\}^{tr}$ .

For normal mode analysis, the disturbance form is

$$\tilde{\mathbf{q}}_1 = \hat{\mathbf{q}}_1(\eta')e^{\alpha\xi' + \beta\zeta' - \omega\tau}, \quad (8)$$

where  $\hat{\mathbf{q}}_1 = \{\hat{u}', \hat{v}, \hat{p}, \hat{T}, \hat{w}\}^{tr}$ .  $\alpha$  and  $\beta$  are wave numbers in the streamwise and spanwise direction respectively.  $\omega$  is a wave frequency. For Görtler instability,  $\beta$  is real. In the calculation of the temporal Görtler mode,  $\alpha$  is set to zero, and complex  $\omega$  becomes an eigenvalue to be solved. For the spatial mode,  $\omega$  is zero and complex  $\alpha$  is solved in the eigenvalue calculation.

When equation (8) is substituted into equation (7), linearized disturbance equations become an eigenvalue

problem of homogeneous system of ordinary differential equations:

$$(\mathbf{A}_0 D^2 + \mathbf{B}_0 D + \mathbf{C}_0)\hat{\mathbf{q}} = 0, \quad (9)$$

where

$$\begin{aligned} \mathbf{A}_0 &= [G'] \\ \mathbf{B}_0 &= [D'] + i\alpha[I'] + i\beta[J'] \\ \mathbf{C}_0 &= [A'] - i\omega[B'] + i\alpha[C'] + i\beta[E'] \\ &\quad - \alpha^2[F'] - \beta^2[H'] - \alpha\beta[L']. \end{aligned} \quad (10)$$

$D$  is the derivative operator in  $\eta'$  direction, i.e.  $D = d/d\eta'$  and  $D^2 = d^2/d\eta'^2$ .

Boundary conditions are subjected to no-slip conditions at the wall, and temperature perturbations are assumed to be vanished at the wall.

$$\hat{u} = \hat{v} = \hat{w} = \hat{T} = 0 \quad \text{at } \eta = 0 \quad (11)$$

$$\hat{u}, \hat{v}, \hat{w}, \hat{T} \rightarrow 0 \quad \text{as } \eta \rightarrow \infty \quad (12)$$

Fourth order finite difference<sup>[20]</sup> and spectral collocation methods<sup>[21]</sup> are applied to discretize the linear system, and the eigenvalue problem is solved numerically by the QR matrix eigenvalue subroutine of the IMSL library.

## 2.2 Direct Numerical Simulation

In the numerical simulation, the three-dimensional Navier-Stokes equations (1) to (4) are written in conservative-law form as follows:

$$\frac{\partial U^*}{\partial t^*} + \frac{\partial F^*_{*j}}{\partial x^*_j} + \frac{\partial F^*_{*vj}}{\partial x^*_j} = 0 \quad (13)$$

where superscript '\*\*' represents dimensional variables and

$$U^* = \{\rho^*, \rho^* u_1^*, \rho^* u_2^*, \rho^* u_3^*, e^*\} \quad (14)$$

$$e^* = \rho^*(C_v^* T^* + \frac{1}{2} u_k^* u_k^*) \quad (15)$$

The flux vectors are

$$F_j^* = \begin{Bmatrix} \rho^* u_j^* \\ \rho^* u_1^* u_j^* + p^* \delta_{1j} \\ \rho^* u_2^* u_j^* + p^* \delta_{2j} \\ \rho^* u_3^* u_j^* + p^* \delta_{3j} \\ (e^* + p^*) u_j^* \end{Bmatrix} \quad (16)$$

$$F_{vj}^* = \begin{Bmatrix} 0 \\ \tau_{1j}^* \\ \tau_{2j}^* \\ \tau_{3j}^* \\ \tau_{jk}^* u_k^* - q_j^* \end{Bmatrix} \quad (17)$$

where

$$\tau_{ij}^* = -\mu^* \left( \frac{\partial u_i^*}{\partial x_j^*} + \frac{\partial u_j^*}{\partial x_i^*} \right) + 2\mu^*/3 \frac{\partial u_k^*}{\partial x_k^*} \delta_{ij} \quad (18)$$

$$q_j^* = -\kappa^* \frac{\partial T^*}{\partial x_j^*} \quad (19)$$

$\mu^*$  is the viscosity coefficient and calculated using the Sutherland's law:

$$\mu^* = \mu_r^* \left( \frac{T^*}{T_r^*} \right)^{3/2} \frac{T_r^* + T_s^*}{T^* + T_s^*} \quad (20)$$

and  $\kappa^*$  is the heat conductivity coefficient computed by assuming a constant Prandtl number  $Pr$ . The gas is assumed to be thermally and calorically perfect gas,

$$p^* = \rho^* R^* T^* \quad (21)$$

where  $R^*$  is the gas constant.

The general curvilinear three-dimensional coordinates  $(\xi, \eta, \zeta, \tau)$  are used along the body fitted grid lines. A shock fitting method is used to treat the bow shock as a computational boundary. The transformation relations for the current grid systems are

$$\begin{cases} \xi = \xi(x, y, z) \\ \eta = \eta(x, y, z, t) \\ \zeta = \zeta(x, y, z) \\ \tau = t \end{cases} \iff \begin{cases} x = x(\xi, \eta, \zeta, \tau) \\ y = y(\xi, \eta, \zeta, \tau) \\ z = z(\xi, \eta, \zeta, \tau) \\ t = \tau \end{cases} \quad (22)$$

where  $\xi_t = 0$  and  $\zeta_t = 0$  because the  $\xi$  and  $\zeta$  grid lines are fixed when the shock boundary moves. In the numerical simulations, the governing equations (13) are

transformed into the computational domain  $(\xi, \eta, \zeta, \tau)$ .

$$\frac{1}{J} \frac{\partial U}{\partial \tau} + \frac{\partial E'}{\partial \xi} + \frac{\partial F'}{\partial \eta} + \frac{\partial G'}{\partial \zeta} + \frac{\partial E'_v}{\partial \xi} + \frac{\partial F'_v}{\partial \eta} + \frac{\partial G'_v}{\partial \zeta} + U \frac{\partial (\frac{1}{J})}{\partial \tau} = 0 \quad (23)$$

The governing equation (23) is discretized in the computational domain  $(\xi, \eta, \zeta, \tau)$ . High order finite difference methods are used for spatial discretization of the equation. Inviscid and viscous flux terms are discretized using different methods: fifth order upwind explicit schemes for the inviscid flux terms and central difference schemes for the viscous terms. For the inviscid flux vectors in governing equation (23), the flux Jacobians contain both positive and negative eigenvalues in general. A simple local Lax-Friedrichs scheme is used to split the inviscid flux vectors into positive and negative wave fields. For example, the flux term  $F'$  in Eq. (23) can be split into two terms of pure positive and negative eigenvalues as follows

$$F' = F'_+ + F'_- \quad (24)$$

where  $F'_+ = \frac{1}{2}(F' + \lambda U)$  and  $F'_- = \frac{1}{2}(F' - \lambda U)$ .  $\lambda$  is chosen to be larger than the local maximum eigenvalues of  $F'$

$$\lambda = \frac{|\nabla \eta|}{J} \left( \sqrt{(\epsilon c)^2 + u'^2} + c \right) \quad (25)$$

where

$$u' = \frac{\eta_x u + \eta_y v + \eta_z w + \eta_t}{|\nabla \eta|} \quad (26)$$

The parameter  $\epsilon$  is a small positive constant added for the smoothness of the splitting. The fluxes  $F'_+$  and  $F'_-$  contain only positive and negative eigenvalues respectively. Therefore, in the spatial discretization of equation (23), the flux derivatives are split into two terms

$$\frac{\partial F'}{\partial \eta} = \frac{\partial F'_+}{\partial \eta} + \frac{\partial F'_-}{\partial \eta} \quad (27)$$

where the first term on the right hand side is discretized by an upwind high-order finite-difference method and the second term by a downwind high-order finite-difference method. Meanwhile, high order central difference schemes are used for the viscous flux terms.

The time advancement of the governing equations is solved by Runge-Kutta schemes.

The fifth-order upwind explicit scheme is

$$u'_i = \frac{1}{h b_i} \sum_{k=-3}^3 a_{i+k} u_{i+k} - \frac{\alpha}{6! b_i} h^5 \left( \frac{\partial u^6}{\partial x^6} \right)_i + \dots \quad (28)$$

where

$$\begin{aligned} a_{i\pm 3} &= \pm 1 + \frac{1}{12}\alpha \\ a_{i\pm 2} &= \mp 9 - \frac{1}{2}\alpha \\ a_{i\pm 1} &= \pm 45 + \frac{5}{4}\alpha \\ a_i &= 0 - \frac{5}{3}\alpha \end{aligned} \quad b_i = 60$$

This scheme is fifth-order upwind scheme when  $\alpha < 0$ , and it is sixth-order central scheme when  $\alpha = 0$ .

The shock fitting method treats the bow shock as a computational boundary at  $\eta = \eta_{max}$ . The flow variables behind the shock are determined by the Rankine-Hugoniot relation across the shock and a characteristic compatibility equation from behind the shock.

### 3 Results

The specific test case is a Mach 15 flow over a blunt wedge with a concave surface. The flow conditions in free stream are

$$\begin{aligned} T_\infty^* &= 101.059K \\ P_\infty^* &= 10.3Pa \\ T_w^* &= 1000K \\ Re_\infty &= \rho_\infty^* U_\infty^* / \mu_\infty^* = 150753.175/m \end{aligned} \quad (29)$$

The body surface is assumed to be a non-slip wall with an isothermal wall temperature  $T_w^*$ . Two-dimensional steady base flow along the blunt body with concave surface is first obtained by two-dimensional simulation. Three-dimensional simulation is carried out for receptivity to freestream and blowing and suction. Figure 1 shows a schematic of the computational domain.

#### 3.1 Steady Base Flow Solutions

In the simulation, the steady base flow is two dimensional while the perturbed flow is three dimensional. The two-dimensional steady flow solutions of

the Navier-Stokes equations for the viscous hypersonic flow over blunt body is simulated using a fifth order explicit upwind shock-fitting scheme. The details of the method and its validations can be found in Ref. [22] and are not discussed here. Grid refinement is used to check the grid independence of the numerical results.

Ten computational zones are used in the two-dimensional steady flow calculations which are resolved by a total of  $1617 \times 121$  grids. Stretched grids are applied in the streamwise and wall normal directions in order to resolve the rapid changes of flow properties near the stagnation point at the blunt nose and in the viscous layers. First three zones are parabolic blunt body given by  $x = by^2 - d$  where  $b$  and  $d$  are the given constants 40.0 and 0.1 respectively. The concave surface is extended in the following zones. The concave body surface is defined by two piecewise-polynomial equations:  $y = a_1 x^3 + a_2 x^2 + a_3 x + a_4$  and  $y = b_1 x^2 + b_2 x + b_3$  where the coefficients are determined to maintain the continuous conditions for the zeroth, first, and second order derivatives of the surface functions. As a result, the current body surface is continuous up to the second order derivatives of the surface functions. More smooth surface can be generated by matching the third order or more, but in our analysis, we match up to the second order in order to get continuous radius curvature which is a function of the first and second order derivatives. For the concave surface, we use relatively large radius of curvature to avoid shock formation due to the compressive waves inside the computational zones. Local Reynolds number is calculated using the flow properties behind the bow shock as  $Re_x = \rho^* U^* x^* / \mu^*$ , where  $\rho^*$ ,  $U^*$ , and  $\mu^*$  are density, velocity, and viscosity respectively, and  $x^*$  is the distance from the blunt nose. Reynolds number ( $Re_x$ ) in the steady base flow calculation is between 0 to  $1.3 \times 10^6$ . Figure 2 shows the distributions of Mach numbers and Görtler numbers along the streamwise direction in concave wall region. Mach number and Görtler number ranges in concave surface are from 6 to 9 and from 4 to 14.7 respectively. For the current test case, the Görtler number increases as  $x$  increases. For the LST analysis, the Görtler mode is unstable when  $G$  is larger than 6. The figure shows Mach number decreases at later zone due to the concave wall. The resulting surface is the blunt body with the convex curve near the leading edge but gradually changes to the concave afterward. The curvature of the concave section is large enough so that the Görtler mode is in unstable region.

Figure 3 shows the numerical solutions of the two-dimensional steady flow. The bow shock shape is obtained as the free stream grid line using a shock fitting method. The numerical solutions for the dimensionless

bow shock normal velocities are in order of  $10^{-8}$  and  $10^{-9}$  which is an indication of the steady state solutions. Pressure in figure 3 is nondimensionalized using the free stream flow variable:  $P_{\infty}^*$ . Pressure contours in the figure show the changes of the flow properties at  $x = 0.35$  which is an indication of the concavity since the concave body surface starts when  $x$  is approximately 0.3. Pressure distributions show that the favorable pressure in convex surface and the adverse pressure for the concave. The result of the adverse gradient is a result of the concave surface which may also have destabilizing effects on the Görtler instability. The surface pressure gradient changes from the favorable to the adverse as the concave wall develops.

### 3.2 Linear Developments of Instability Waves

Having obtained the two-dimensional steady base flow solutions, spatial linear stability analysis for the computed two-dimensional steady base flow is applied to find instability waves. In the LST analysis, spanwise wave number  $\beta$  is given, and complex  $\alpha$  and corresponding eigenfunctions are computed in the eigenvalue calculations for various frequencies. Figure 2 shows the Görtler number increases almost linearly with respect to  $x$ . At low Görtler number, there is no unstable Görtler modes. The unstable modes appear approximately at  $G = 6$ , and LST analysis is applied at  $G = 6.8$  and  $x = 1.0$  for various frequencies ( $\omega$ ).

Görtler vortices are spatially growing steady vortices. LST analysis showed that Görtler mode appears at zero forcing frequency ( $\omega = 0$ ), but as frequency increases, the mode disappears and other instability modes (first mode, second mode, third mode, etc) develop at  $x = 1.0$ . It is found that when nondimensional  $\beta$  is 0.1, the growth rate of Görtler mode is maximum, and  $\beta$  is fixed as 0.1 for all instability modes. However, LST results showed that only Görtler mode is unstable and other modes are stable. Figure 4 shows streamwise wave numbers ( $\alpha_r$ ) and growth rates ( $\alpha_i$ ) for Görtler mode, first mode, second mode, and third mode at various forcing frequencies. Görtler vortices are longitudinal counter rotating vortices which develop in streamwise direction. Therefore,  $\alpha_r$  is zero for Görtler mode and non-zero for other instability modes. Figure 4 also shows that growth rates of all modes except for Görtler modes are positive. Positive growth rates represent the stable modes. LST results at  $x = 1.0$  shows that Görtler mode is the most dangerous mode which grows as flow moves downstream.

Figure 5 shows the eigenfunctions of Görtler mode

obtained by LST at  $x = 1.0$  and  $\beta = 0.1$ . Flow properties are nondimensionalized by free stream values such as streamwise velocities by  $U_{\infty}^*$ , normal and spanwise velocities by  $U_{\infty}^*/\sqrt{Re_x}$ , temperature by  $T_{\infty}^*$ , length scales by  $x^*$  at  $G = 6.8$ . The growth rate ( $\alpha_i$ ) of the primary Görtler mode is -1.014 which is unstable.

Figure 6 shows the eigenfunctions of pressure disturbances for boundary-layer modes. The nondimensional forcing frequency ( $\omega$ ) for first, second, and third modes are 40.0, 80.0 and 130.0 respectively. Streamwise wave number and growth rates for each modes are represented in figure 4 by (1), (2) and (3). Mack<sup>[23]</sup> showed that the number of zeros in  $p_r$  is one less than the mode number. It is well represented in figure 6: no-zeros for first mode, one-zero for second mode, and two-zeros for third mode.

Having obtained instability modes using LST analysis, the modes are imposed at  $x = 1.0$ , and the three-dimensional simulation is set up in a sectional computational domain shown in figure 1. The simulated results are compared with those obtained by LST for code validation.

DNS study of linear development of Görtler mode is first considered since it is the most unstable mode in our computational domain. Weak disturbances of Görtler mode are introduced to the base flow at the entrance of the computational domain located at  $x = 1.0$ . Inlet Görtler number and local Reynolds number is 6.8 and  $4.23 \times 10^5$  respectively. One computational domain (zone 7) is used for the linear development of the Görtler modes. The range of Görtler number is 6.8 to 8.5. Amplitudes of the disturbances are the order of  $10^{-6}U_{\infty}$  so that the Görtler mode is linear. The results from DNS are compared with those predicted by LST.

In the DNS, a Fourier collocation method is applied to the spanwise direction since Görtler vortices are periodic in the spanwise direction. For the simulation of the linear development of Görtler vortices, four collocation points are used to compute one spanwise wave length of the disturbances. Four collocation points are enough to resolve the linear growth of the Görtler modes in spectral analysis because the four points can resolve mean flow and the fundamental mode.

Figure 7 shows temperature perturbation contours of the Görtler mode after it reaches a steady state condition. The growth of Görtler vortices in the streamwise direction is shown by the intensity of the disturbances. The variables in the figure are nondimensionalized in the following: velocities by  $U_{\infty}^*$ , temperature by  $T_{\infty}^*$ , and length by  $X_0^*$  of zone 7. In figure 7, DNS results of temperature disturbance contours and wall normal dis-

tributions are compared with those from LST located at  $x = 1.15$  and  $G = 7.57$ . Solid lines represent the simulated results, and dashed lines are those from LST. The simulated results are compared well with those obtained from LST.

Boundary-layer modes are also studied by solving the full Navier-Stokes equations. Eigenfunctions and corresponding forcing frequency of the modes are introduced at the entrance of computational domain. The disturbances propagate spatially and reaches periodic conditions. Figure 8 shows instantaneous pressure perturbations of first mode after it reaches periodic condition. Non-dimensional forcing frequency is 40.0 which is normalized by velocity behind shock at the inlet of computational domain and streamwise distance from blunt leading edge to the inlet. Instantaneous streamwise cross sectional contours ((a)) clearly show the development of one peak pressure structure which is characteristic of first mode. The development of first mode is also well represented in the spanwise cross sectional contours shown in figure 8 (b). Dashed line indicates negative values of pressure perturbations. Figure 8 (c) is instantaneous streamwise distributions of surface pressure disturbances. LST analysis shows that first mode is stable in our computational domain at  $\omega = 40.0$ . Amplitude of surface pressure perturbations decays in the streamwise direction which indicates the mode is stable.

Second and third modes obtained from LST are also imposed at the entrance of computational domain. Non-dimensional inlet forcing frequency of second and third modes are 80.0 and 130.0 respectively. In each cases, disturbances propagate spatially and reach periodic conditions. Figure 9 shows the instantaneous pressure disturbances of second mode after it reaches periodic condition. Two-peaks structure of second mode pressure disturbances are well represented in figure 9 (a) and (b). Imposed disturbances are stable, and figure 9 (c) shows the decaying disturbances. Similar results are observed in development of third mode shown in figure 10. Three-peaks structure of third mode pressure distribution and spatially decaying disturbances are well represented in the figure.

Fourier analysis is carried out on the numerical solution of instability modes after they reach the periodic conditions. Fourier transform of a disturbance variable is expressed to:

$$q'(x, y, z) = \sum_{m=0}^M \sum_{n=0}^N |q'_n| e^{i[m\beta z - n\omega t + \phi_n]} \quad (30)$$

where  $\beta$  and  $\omega$  is the spanwise wave number and fre-

quency of inlet disturbance respectively, and  $q'(x, y, t)$  represents any perturbation variables.  $|q'_n(x, y)|$  and  $\phi_n(x, y)$  are the local perturbation amplitudes and phase angles respectively. The integer  $m$  and  $n$  represents the wave modes of the perturbation fields.  $(m, n) = (1, 1)$  represents a fundamental mode. Wave number ( $\alpha_r$ ) of the fundamental mode can be calculated using:

$$\alpha_r = \frac{\partial |\phi_1|}{\partial x} \quad (31)$$

Figure 11 compares wave numbers for three instability modes obtained from Fourier analysis of numerical solutions and LST analysis in whole computational domain. Wave numbers are nondimensionalized by streamwise distance from blunt leading edge to the inlet of computational domain. Simulated results are compared well with those obtained by LST analysis. The figure also shows that the higher instability mode has larger wave number which represent shorter wave length. Eigenfunctions obtained by Fourier analysis are also compared with those from LST analysis. Figure 12 shows real and imaginary parts of pressure disturbances of three instability waves at  $x = 1.15$  obtained by Fourier and LST analysis. All three cases are compared well.

### 3.3 Blowing and Suction

Engine inlet contains concave surface, and air and fuel is mixed near inlet which may impose disturbances into the boundary layers. Such disturbances can be studied using blowing and suction. Figure 13 shows a schematic of the engine inlet with blowing and suction. Using computed 2-D base flow, blowing and suction is applied at inlet of zone 7 which disturbs flow, but net amount of incoming flow is zero. Since Görtler mode is steady, steady blowing and suction is investigated. Boundary condition of normal velocity at the surface is as follows:

$$v^* = \cos(\beta^* z) \times f(x), \quad (32)$$

where nondimensional  $\beta$  is 0.1, and length of  $z$  is one wavelength of the vorticity. Figure 14 shows an amplitude function,  $f(x)$ , which gives small slot at the surface in which disturbances are imposed by blowing and suction. Eq.(32) is independent of time and imposes disturbances with spanwise wave number.  $\beta$ , into hypersonic boundary layers.

Figure 15 and 16 show cross sectional disturbance contours after they reach steady state condition. Fig-

ure 15 are the contours at several different streamwise cross section. Blowing and suction is located a little away from the inlet, so there is no disturbances at the inlet. The figure shows Görtler mode development. One peak point of streamwise ( $u$ ) and normal ( $v$ ) velocity disturbances and two peak points of the temperature are well represented in the figure which are the characteristics of Görtler mode. However, the figure also shows Mach wave development outside boundary layers. Spanwise cross sectional contours in figure 16 shows that disturbances induced by blowing and suction creates Mach wave as well as Görtler mode. The contours show the development of streamwise vorticity layer inside boundary layers which is Görtler vortices. However, other disturbances outside boundary layers with a certain angle with respect to the body surface also appear in the contours. We examined the wave angle and realized that it is Mach wave angle. Such Mach wave is relatively strong compared with Görtler mode inside boundary layers, and it makes difficulties of Görtler mode development inside boundary layers.

### 3.4 Receptivity to Freestream Disturbance Waves

In this section, forcing disturbances are imposed by receptivity to freestream disturbance waves. The wave fields are represented by perturbations of instantaneous flow variables with respect to the local steady base flow variables at the same location. There are four kinds of weak perturbation waves in a uniform flow in the freestream: fast acoustic waves, slow acoustic waves, entropy waves, and vorticity waves. The perturbation of an arbitrary flow variables can be written in the following form:

$$q'_{\infty} = |q_{\infty}| e^{i(\mathbf{k}_{\infty} \cdot \mathbf{x} - \omega t)} \quad (33)$$

where  $q'_{\infty}$  represents the perturbation of any flow variable,  $|q_{\infty}|$  is the wave amplitude constant,  $\mathbf{k}_{\infty}$  is the wavenumber, and  $\omega$  is the wave frequency in the freestream before reaching the shock. In this paper, we have studied fast acoustic waves and vorticity waves. Perturbation amplitudes of non-dimensional flow variables satisfy the following dispersion relations:

fast acoustic waves ( $\omega = \mathbf{U}_{\infty} \cdot \mathbf{k}_{\infty} + c_{\infty} k$ ):

$$\begin{aligned} |\rho'|_{\infty} &= |\rho'|_{\infty} / \gamma = \epsilon M_{\infty} , \\ |u'|_{\infty} M_{\infty} k_x / k &= |w'|_{\infty} M_{\infty} k_z / k = \epsilon M_{\infty} , \\ |s'|_{\infty} &= |v'|_{\infty} = 0 ; \end{aligned}$$

streamwise vorticity waves ( $\omega = \mathbf{U}_{\infty} \cdot \mathbf{k}_{\infty}$ ):

$$\begin{aligned} |v'|_{\infty} M_{\infty} k_y / k &= |w'|_{\infty} M_{\infty} k_z / k = \epsilon M_{\infty} , \\ |u'|_{\infty} &= |p'|_{\infty} = |s'|_{\infty} = 0 ; \end{aligned}$$

where  $\epsilon$  is a small number, and  $\epsilon M_{\infty}$  represents the relative amplitude of a freestream wave. The parameter  $k$  is the freestream wavenumber.

#### 3.4.1 Fast Acoustic Waves

Fast acoustic waves with wave angle,  $\theta_{ac}$ , enter the top computational boundary starting at the inlet of Zone 5 in which surface shape is concave. Wavenumbers of streamwise and spanwise components are as follows:

$$k_x = k \cos(\theta_{ac}) , k_z = k \sin(\theta_{ac}) \quad (34)$$

Two different wave angles ( $\theta_{ac}$ ) are investigated: 30° and 90°.

Figure 17 shows the instantaneous streamwise velocity perturbation contours for two different wave angles. In the case of  $\theta_{ac} = 90^\circ$  in which waves propagate spanwise direction only, much stronger disturbance develops inside hypersonic boundary layers compared with the case of  $\theta_{ac} = 30^\circ$ . It shows that the concave surface has more influences on spanwise disturbance than on the streamwise. In addition, at  $\theta_{ac} = 90^\circ$ , streamwise wavenumber is zero which gives much smaller frequency compared with the one for  $\theta_{ac} = 30^\circ$ . Görtler mode is standing wave induced by spanwise disturbances. The figure shows that waves with lower frequency directed more spanwise direction induce strong disturbance development inside boundary layer. Figure 18 shows instantaneous spanwise cross sectional streamwise disturbance contours for two different  $\theta_{ac}$ . The figure shows that in both cases, freestream acoustic waves do not reach to boundary layer. 30° acoustic waves do not induce disturbance inside boundary layer since disturbances induced by the acoustic waves are T-S waves which develop after the wave reach the boundary layer. However, 90° acoustic waves create disturbance inside boundary layer before they reach the boundary layer which is associated with Görtler mode induced by concave surface. Figure 19 shows wall normal distributions of streamwise velocity perturbations at three different streamwise locations obtained from Fourier analysis. While 30° acoustic waves induce disturbances inside boundary layer whose amplitudes are one order lower than those for acoustic waves, the amplitudes for the 90° are the same order of magnitude of

those for the acoustic waves. Also the amplitudes for the  $90^\circ$  increase as flow moves downstream. Freestream receptivity to fast acoustic waves shows that disturbances inside boundary layer induced by the acoustic waves in spanwise direction with low wave frequency are more affected by the concave surface which is associated with Görtler vortices.

### 3.4.2 Vorticity Waves

#### Results

In the 2-D base flow we have investigated so far, only Görtler mode is unstable. LST analysis shows that all other modes such as Mack's modes are stable in our computational domain, and we have simulated the new sets of 2-D steady base flow with ten times higher Reynolds number. In the simulation, we have enlarged the blunt body ten times with the same flow conditions in freestream. Reynolds number of the resulting 2-D base flow is ten times larger than the previous. Six computational zones are used in the new two-dimensional steady flow calculations which are resolved by a total of  $1933 \times 241$  grids. Figure 20 shows the numerical solutions of the two-dimensional steady flow. Pressure in figure 20 is nondimensionalized using the free stream flow variable:  $P_\infty^*$ . Basic structure of the pressure is similar to the one in figure 3, but Reynolds number is ten times larger. The figure also shows the adverse pressure gradient in concave region. Having obtained the new 2-D base flow, spatial linear stability analysis for the computed two-dimensional steady base flow is applied at the end of the computational domain to find instability waves. In the LST analysis, spanwise wave number  $\beta$  is given, and complex  $\alpha$  and corresponding eigenfunctions are computed in the eigenvalue calculations for various frequencies. At zero wave frequency ( $\omega$ ), we found unstable Görtler modes at the end of the computational domain. We have also investigated Mack's modes at various frequencies. Figure 21 shows the growth rates ( $\alpha_i$ ) for various wave modes with respect to wave frequencies. Growth rates and frequencies are nondimensionalized by streamwise velocity behind the shock and streamwise distance. At this location, there is unstable frequency range for *Mode I*, but other modes are still stable. For the high Reynolds number base flow, we also found other modes indicated 1 and 2 in the figure which could not be found in the lower Reynolds number. However, those modes are stable than Mode I, II and III, and at this location, Görtler mode is still most unstable. In order to investigate these modes, we conducted receptivity to freestream disturbances. In this study, we imposed freestream disturbances near the leading edge in order to study leading edge effects.

Some instability modes such as the first mode appear near the leading edge and develop downstream, and disturbances imposed a little far away from the edge may not excite such modes. Therefore, in this case, we conducted freestream receptivity near the leading edge.

First, we have investigated receptivity to freestream streamwise vorticity waves. Acoustic waves enters boundary layers and excite T-S waves, therefore, fast acoustic wave studies in previous section, pure Görtler mode could not be obtained. Görtler vortices may be excited by freestream vorticity waves, and we imposed streamwise freestream vorticity waves to the 2-D base flow solution. In the freestream, nonzero disturbance variables are normal and spanwise velocity disturbances ( $v'$  and  $w'$ ) and wavenumbers ( $k_y$  and  $k_z$ ). Amplitudes of other disturbances and streamwise wavenumber are zero. Zero streamwise wavenumber gives zero wave frequency. Resulting freestream waves are streamwise vorticity with zero frequency which is the characteristics of Görtler vortices inside boundary layers. Figure 22 shows streamwise velocity perturbation contours of the first two computational zones. The figure shows that freestream vorticity waves enter the computational domain at top boundary. The figure also shows that vorticity layer also exist inside boundary layer which is induced by vorticity waves entered near the leading edge. We have simulated all six computational zones for vorticity wave propagation. Concave surface is in last three zones, and adverse pressure gradient region develops in last two computational zones. Figure 23 shows surface shape of the blunt body and streamwise distributions of streamwise velocity and temperature perturbation inside boundary layers. The figure shows that the disturbances increase near the leading edge due to the leading edge effects, but decay before they reach the concave surface region. Concave surface starts at  $x \approx 4$  as shown in figure 23, and the amplitudes of disturbances amplify in concave region which may be associated with Görtler mode. LST analysis shows that unstable Görtler mode appears at the end of the computational domain, so DNS results could not be verified by LST; however concave surface excite steady streamwise vorticity waves while the convex stabilize the waves. It is the same phenomena of Görtler vortices.

#### Continuing Simulation

Beam of vorticity waves with amplitude using shape function shown in figure 14 imposed at top boundary is simulating since it is more appropriate for experimental comparison. Work is also in progress to investigate frequency effects of vorticity waves. LST analysis showed that at low frequency ( $\omega \approx 50$  (figure 21)), there

is unstable Mode I in the concave region. Freestream vorticity waves with the unstable forcing frequency will be simulated to study if unsteady vorticity waves can excite unstable T-S waves. Receptivity to freestream acoustic waves with the same frequency will also be simulated for the comparison.

## 4 Summary and Future Works

The main focus of this paper is to study receptivity of Görtler vortices and its interactions with other environmental disturbances using Direct Numerical Simulation. Eigenfunctions of Görtler and other instability modes from LST analysis were imposed at the inlet of the computational domain. Subsequent development of the modes were carried out by solving the full Navier-Stokes equations. The DNS results were compared with those from LST for a code validation. There were good agreements between the two results. Blowing and suction in concave region introduced spanwise disturbance in hypersonic boundary layers and develop Görtler mode inside the boundary layer. The simulation of fast freestream acoustic waves imposed at bow shock in concave region showed that the spanwise direction acoustic waves with low frequency excite more Görtler vorticity kind of disturbances inside boundary layer than the streamwise direction. We also investigated steady streamwise vorticity waves imposed at bow shock near the leading edge. The results showed vorticity waves inside boundary layers amplify in the concave region while decay in the convex region which is associated with Görtler vortices.

LST analysis for 2-D high Reynolds number steady base flow showed that there is unstable mode other than Görtler mode although LST results showed that Görtler mode is still the most dominant instability in Mach 15 flow over a blunt wedge with concave surface. We will verify this using receptivity to freestream acoustic waves which applied from the leading edge to the concave region. For the vorticity waves, we will extend computational domain in streamwise direction in order to study the instability effects of vorticity waves in the concave region since the simulation showed that vorticity waves inside boundary layer start to amplify dramatically. The frequency effects of the vorticity waves will also be investigated. In this paper, we assumed streamwise wave number is zero in freestream vorticity wave simulation, but if there is non zero streamwise wave number, wave frequency is not zero, and we will study the frequency effects on instability induced by freestream vorticity waves.

## Acknowledgments

This work was sponsored by the Air Force Office of Scientific Research, USAF, under AFOSR Grant # F49620-00-1-0101 monitored by Dr. John Schmisser. The views and conclusions contained herein are those of the author and should not be interpreted as necessarily representing the official policies or endorsements either expressed or implied, of the Air Force Office of Scientific Research or the U.S. Government. The numerical simulations were performed on the IBM SPs at cfdlab in UCLA and at the NAVO MSRC.

## References

- [1] Görtler, H., "Instabilität umt laminarer Grenzschichten an Konkaven Wänden gegenüber gewissen dreidimensionalen Störungen," *ZAMM*, Vol. 21, 1941, pp. 250-52.
- [2] Tani, I., "Production of longitudinal vortices in the boundary layer along a concave wall," *J. Geophysical Res.*, Vol. 67 no 8, 1962, pp. 3075-80.
- [3] Aihara, Y., "Görtler vortices in the nonlinear region," In *Theoretical and Experimental Fluid Mechanics*, ed U. Müller, K. G. Roesner, B. Schmidt, pp 331-38. Berlin:Springer-Verlag, 1979.
- [4] Peerhossaini, H. and Wesfreid, J. E., "Experimental study of the Taylor-Görtler Instability," In *Propagation in Systems Far From Equilibrium*, ed J. E. Wesfreid, H.R. Brand, D. Manneville, G. Albinet, N. Boccara, et al, pp. 399-412. Berlin:Springer-Verlag, 1988.
- [5] Aihara, Y. and Koyama, H., "Nonlinear development and secondary instability of Görtler Vortex," In *Stability in the Mechanics on Continua*, ed F. H. Schroeder, pp 345-54. Berlin: Springer-Verlag, 1982.
- [6] Aihara, Y., Tomita, Y., and Ito, A., "Generation, development and distortion of longitudinal vortices in boundary layers along concave and flat plates," In *Laminar-Turbulent Transition*, ed V. V. Kozlov, pp. 447-54. New York:Springer-Verlag, 1985.
- [7] Swearingen, J. D. and Blackwelder, R. F., "The growth and breakdown of streamwise vortices in the presence of a wall," *J. Fluid Mech.*, Vol. 182, 1987, pp. 255-290.
- [8] Hall, P., "The nonlinear development of Görtler vortices in growing boundary layers," *J. Fluid Mech.*, Vol. 193, 1988, pp. 243-66.

- [9] Lee, K. and Liu, T. C., "On the growth of mushroomlike structure in nonlinear spatially developing Görtler vortex flow," *Phys. Fluids A*, Vol. 4(1), 1992, pp. 95-103.
- [10] Liu, W. and Domaradzki, J. A., "Direct numerical simulation of transition to turbulence in Görtler flow," *J. Fluid Mech.*, Vol. 246, 1993, pp. 267-299.
- [11] Yu, X. and Liu, T. C., "On the mechanism of sinuous and varicose modes in three-dimensional viscous secondary instability of nonlinear Görtler rolls," *Phys. Fluids*, Vol. 6(2), 1994, pp. 736-50.
- [12] Li, F. and Malik, M., "Fundamental and subharmonic secondary instabilities of Görtler vortices," *J. Fluid Mech.*, Vol. 297, 1995, pp. 77-100.
- [13] Nayfeh, A. H., "Effect of streamwise vortices on Tollmien-Schlichting waves," *J. Fluid Mech.*, Vol. 107, 1981, pp. 441-453.
- [14] Malik, M. R., "Wave interaction in three dimensional boundary layers," *AIAA Paper 86-1129*, 1986.
- [15] Nayfeh, A. H. and Al-Maaitah, A., "Influence of streamwise vortices on Tollmien-Schlichting waves," *Phys. Fluids*, Vol. 31(12), 1988, pp. 3543-3549.
- [16] Malik, M. R. and Hussaini, M. Y., "Numerical simulation of interaction between Görtler vortices and Tollmien-Schlichting waves," *J. Fluid Mech.*, Vol. 210, 1990, pp. 183-199.
- [17] Danier, J. P., Hall, P., and Seddougui, S. O., "On the receptivity problem for Görtler vortices: vortex motion induced by wall roughness," *Phil. Trans. R. Soc. Lond. A*, Vol. 335, 1991, pp. 51-85.
- [18] Lin, R., Malik, M. R., and Sengupta, R., "Computation of hypersonic boundary-layer response to external disturbances," *AIAA 99-0411*, 1999.
- [19] Zhong, X., "Leading-edge receptivity to free-stream disturbance waves for hypersonic flow over a parabola," *J. Fluid Mech.*, Vol. 441, 2001, pp. 315-367.
- [20] Hu, S. and Zhong, X., "Linear stability of viscous supersonic plane Couette flow," *Phys. Fluids*, Vol. 10(3), 1998, pp. 709-729.
- [21] Malik, M. R., "Numerical methods for hypersonic boundary layer stability," *J. Comput. Phys.*, Vol. 86, 1990, pp. 376-413.
- [22] Zhong, X., "High-order finite-difference schemes for numerical simulation of hypersonic boundary-layer transition," *J. Comput. Phys.*, Vol. 144, 1998, pp. 662-709.
- [23] Mack, L. M., "Boundary layer linear stability theory," *AGARD Rep. No. 709*, 1984.

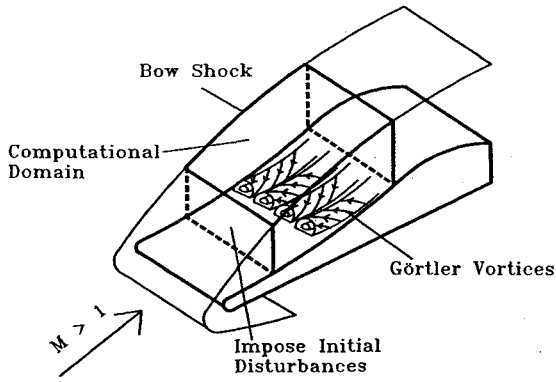


Figure 1: A schematic of computational domain of two-dimensional base flow and three-dimensional Görtler instability simulation.

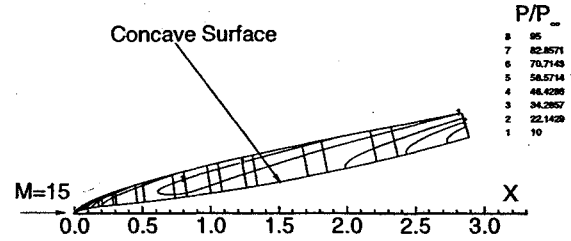


Figure 3: Temperature (upper figure) and pressure (lower figure) contours for the steady two-dimensional base flow at  $M_\infty = 15$  and  $Re_\infty = 150753.17$ .

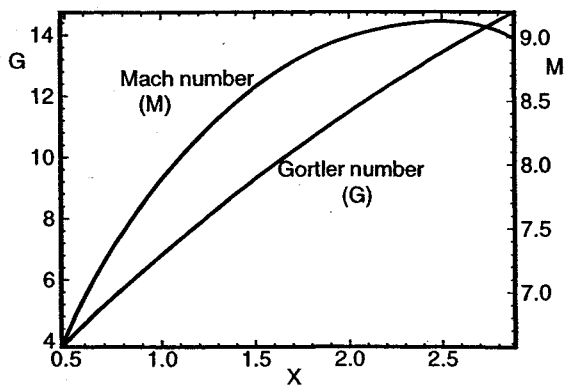


Figure 2: Distributions of Görtler number and Mach number behind shock. Görtler number increases since Reynolds number increases.

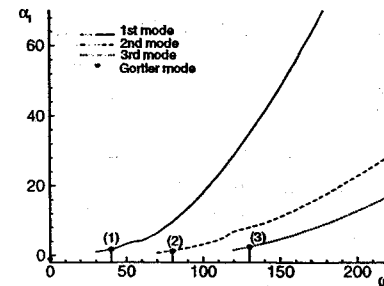
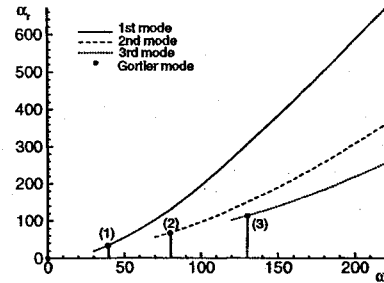


Figure 4: Streamwise wave number and growth rates for instability modes obtained by LST analysis at  $x = 1$ ,  $G = 6.8$ ,  $M = 7.89$ ,  $Re_x = 4.23 \times 10^5$ , and  $\beta = 0.1$ .

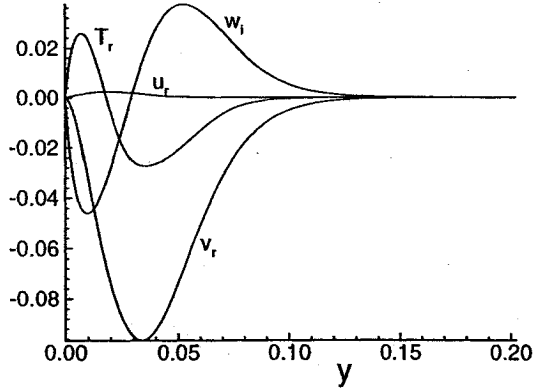


Figure 5: Eigenfunctions of Görtler mode obtained by LST analysis at  $x = 1$ ,  $G = 6.8$ ,  $M = 7.89$ ,  $Re_x = 4.23 \times 10^5$ , and  $\beta = 0.1$ .

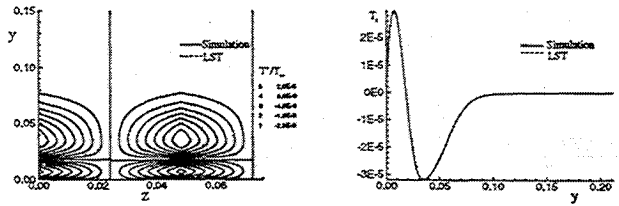
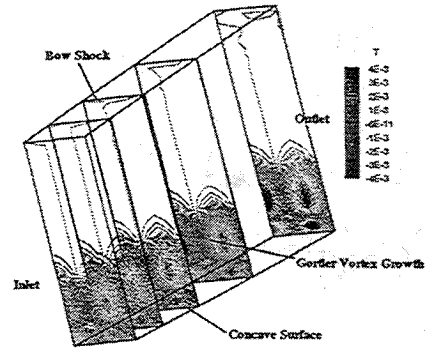


Figure 7: Temperature perturbation contours of the primary Görtler mode at  $x = 1.15$  and  $G = 7.57$ . DNS results compare well with those from LST

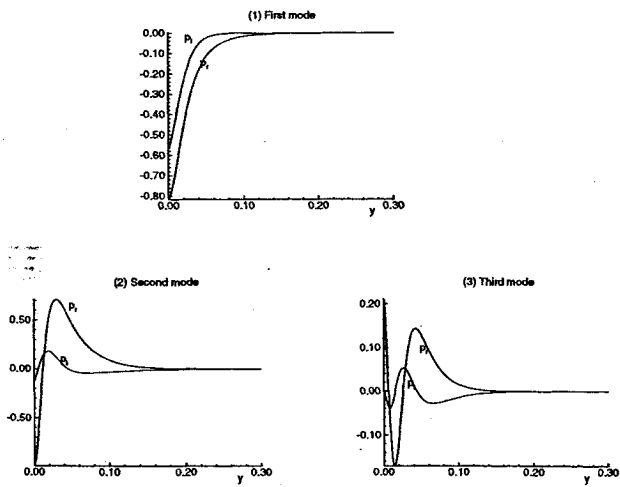
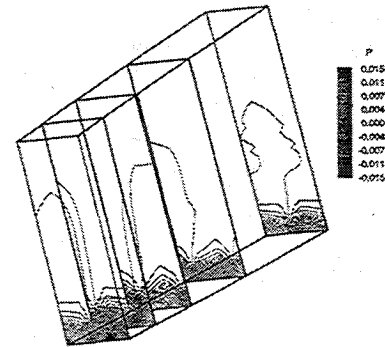
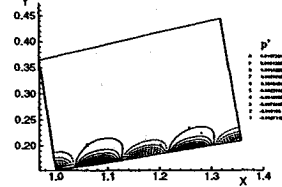


Figure 6: Eigenfunctions of pressure disturbances for boundary-layer modes obtained by LST analysis at  $x = 1$ ,  $G = 6.8$ ,  $M = 7.89$ ,  $Re_x = 4.23 \times 10^5$ , and  $\beta = 0.1$ .

(a) Pressure Contours



(b) Pressure Contours in XY plane



(c) Streamwise Distributions

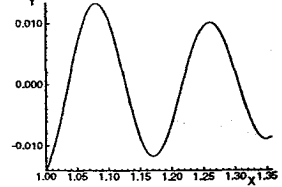


Figure 8: Instantaneous pressure disturbances distributions of first mode after it reaches periodic conditions

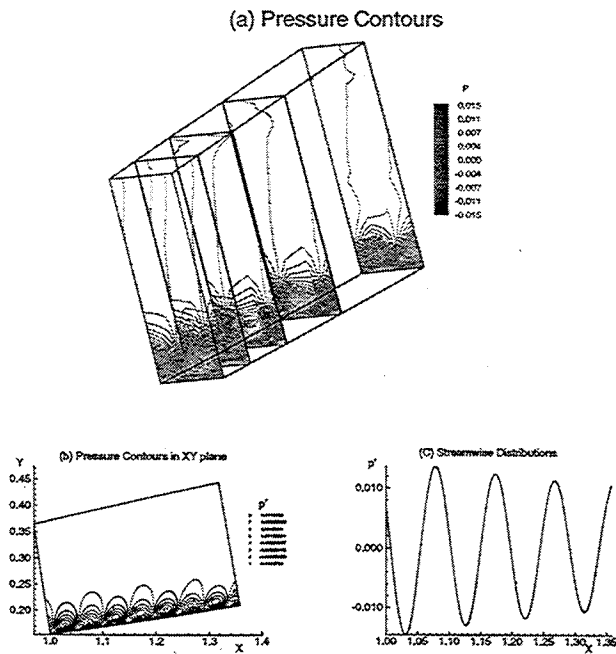


Figure 9: Instantaneous pressure disturbances distributions of second mode after it reaches periodic conditions

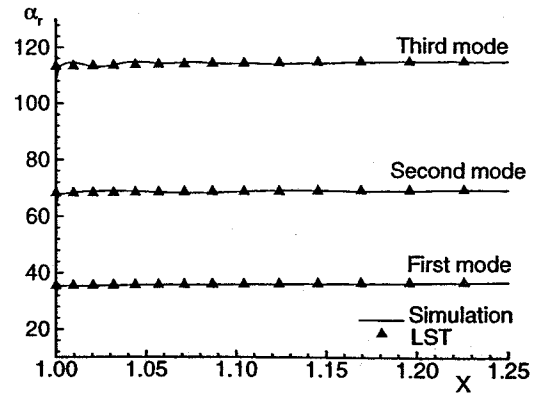


Figure 11: Comparison of instability modes wave number obtained from DNS with LST for whole computational domain

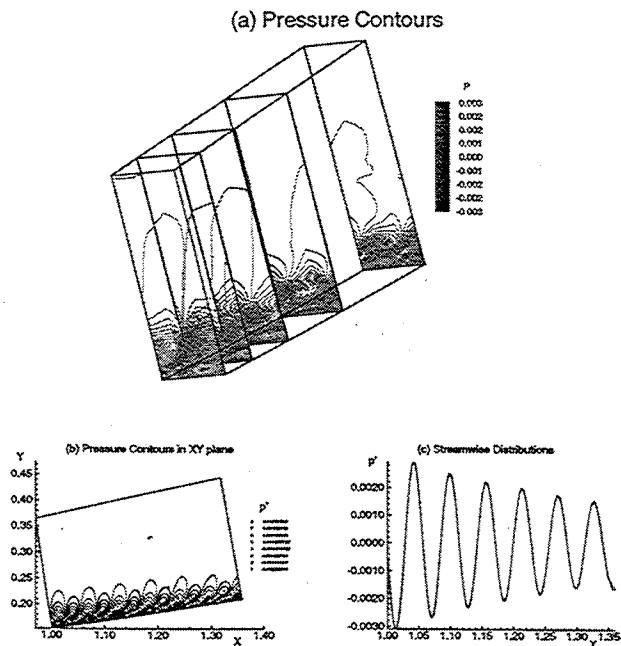


Figure 10: Instantaneous pressure disturbances distributions of third mode after it reaches periodic conditions

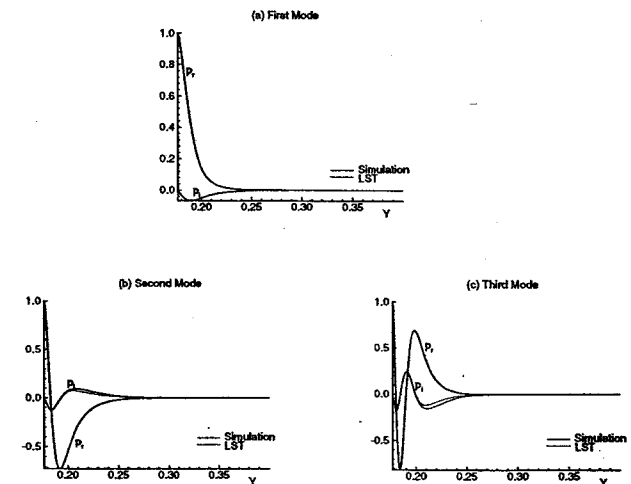


Figure 12: Eigenfunctions comparison of DNS results with LST results at  $x = 1.15$  and  $G = 7.57$ .

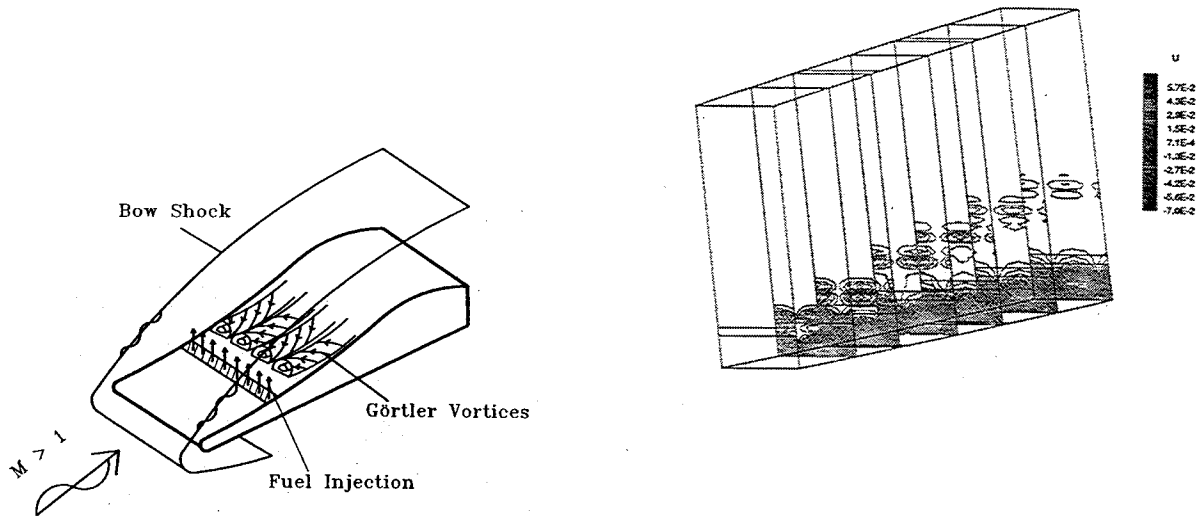


Figure 13: A schematic of the concave body(engine inlet) on and Görtler vortices exist. Fuel injection is placed in front of the vortices.

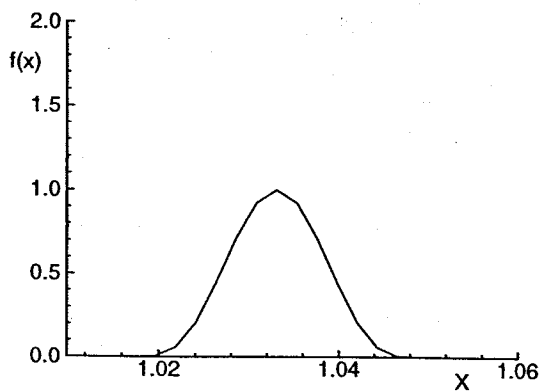
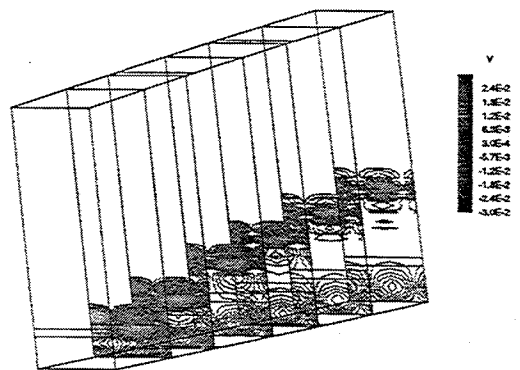
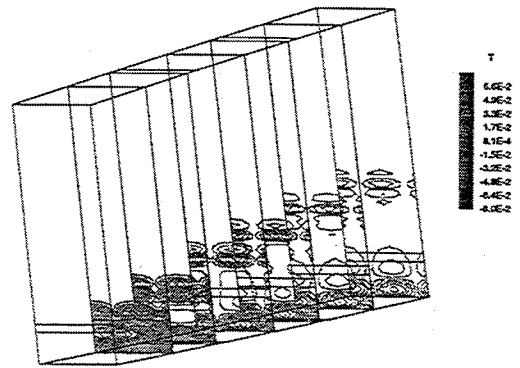
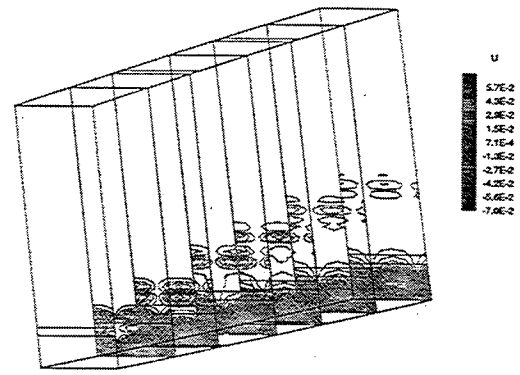


Figure 14: Amplitude function of steady blowing and suction.

Figure 15: Streamwise cross sectional disturbance contours induced by steady blowing and suction. Görtler mode develops in hypersonic boundary layers.

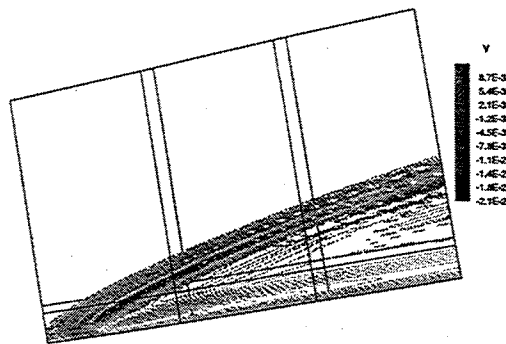
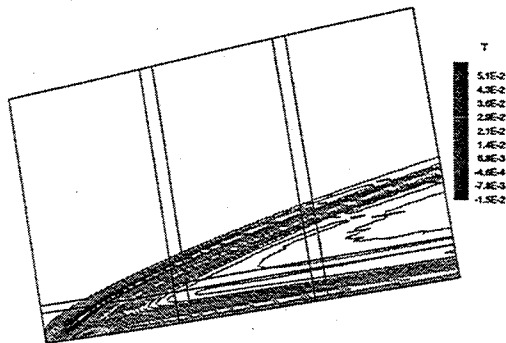
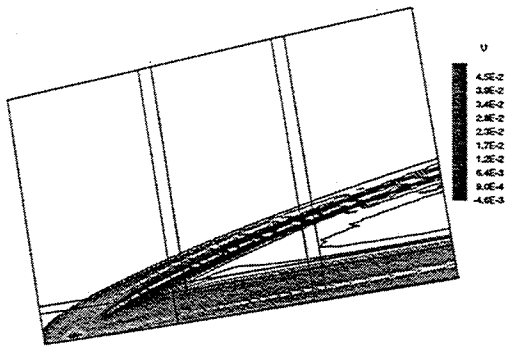


Figure 16: Spanwise cross sectional disturbance contours induced by steady blowing and suction. Mach wave also develops induced by blowing and suction.

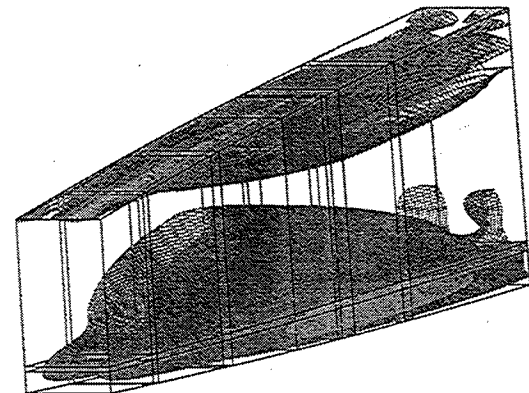
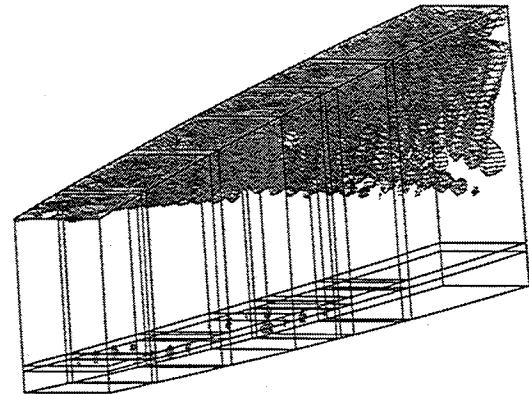


Figure 17: Instantaneous streamwise velocity perturbation contours induced by freestream fast acoustic waves:  $\theta_{ac} = 30^\circ$  (up) and  $90^\circ$  (down).

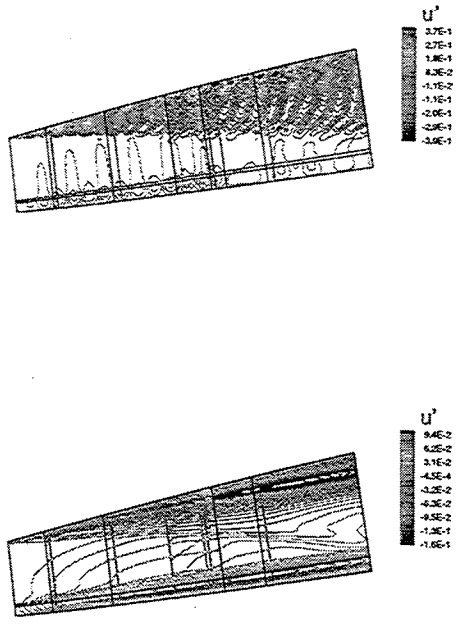


Figure 18: Instantaneous spanwise cross sectional streamwise velocity perturbation contours induced by freestream fast acoustic waves:  $\theta_{ac} = 30^\circ$  (up) and  $90^\circ$  (down).

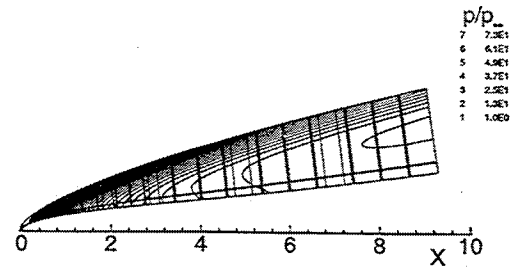


Figure 20: Pressure contours of 2-D numerical solution for high Reynolds number at  $M_\infty = 15$ .

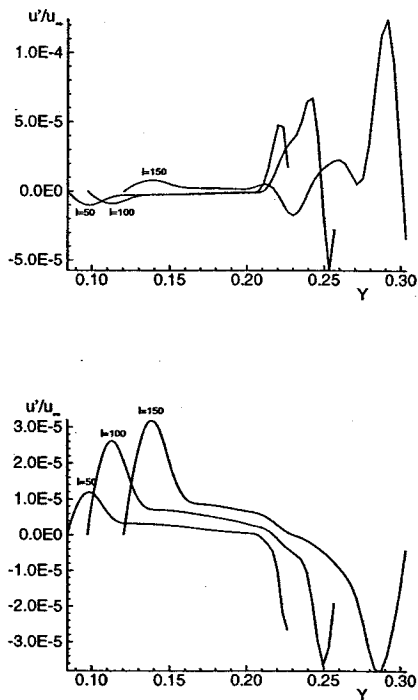


Figure 19: Wall normal distributions of streamwise velocity perturbation at three different streamwise locations obtained by Fourier analysis:  $\theta_{ac} = 30^\circ$  (up) and  $90^\circ$  (down).

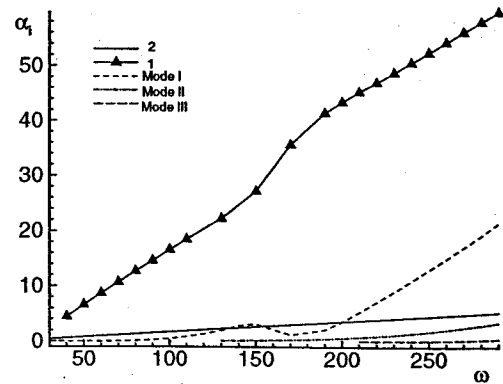


Figure 21: The growth rates ( $\alpha_i$ ) for various wave modes with respect to wave frequencies at the end of the computational domain.

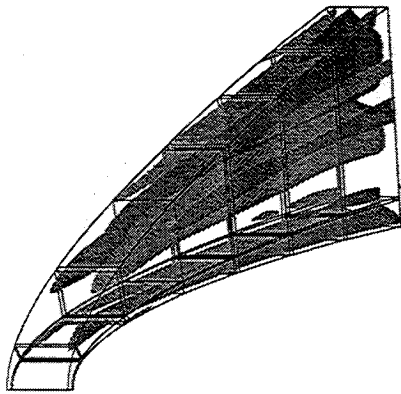


Figure 22: Streamwise velocity perturbation contours of the first two computational zones. The figure shows that freestream vorticity waves enter the computational domain at top boundary.

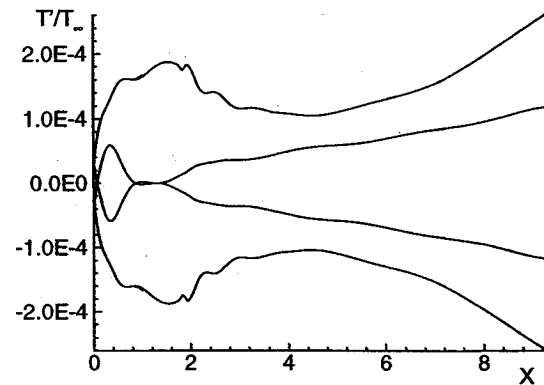
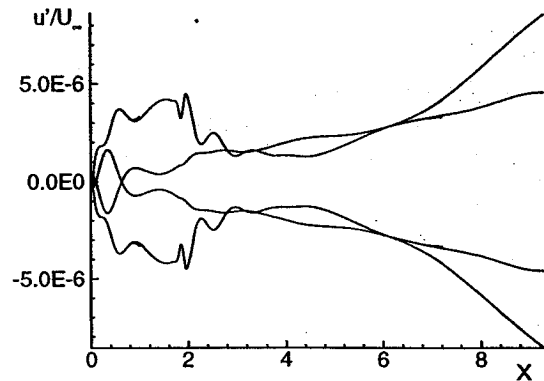
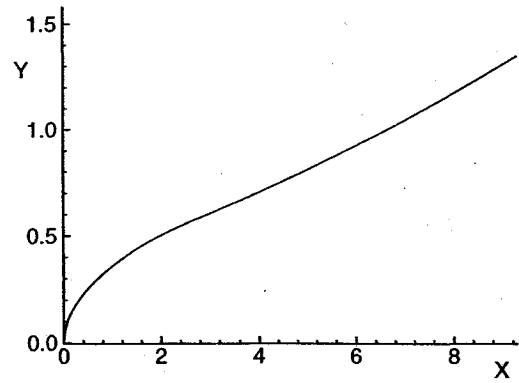


Figure 23: Surface shape and streamwise distributions of streamwise velocity and temperature perturbation induced by steady freestream vorticity waves.